

Journal of Astronomical Telescopes, Instruments, and Systems

AstronomicalTelescopes.SPIEDigitalLibrary.org

Design, implementation, and performance of the Astro-H SXS calorimeter array and anticoincidence detector

Caroline A. Kilbourne
Joseph S. Adams
Regis P. Brekosky
James A. Chervenak
Meng P. Chiao
Megan E. Eckart
Enectali Figueroa-Feliciano
Masimilliano Galeazzi
Christoph Grein
Christine A. Jhabvala
Daniel Kelly
Maurice A. Leutenegger
Dan McCammon
F. Scott Porter
Andrew E. Szymkowiak
Tomomi Watanabe
Jun Zhao

Caroline A. Kilbourne, Joseph S. Adams, Regis P. Brekosky, James A. Chervenak, Meng P. Chiao, Megan E. Eckart, Enectali Figueroa-Feliciano, Masimilliano Galeazzi, Christoph Grein, Christine A. Jhabvala, Daniel Kelly, Maurice A. Leutenegger, Dan McCammon, F. Scott Porter, Andrew E. Szymkowiak, Tomomi Watanabe, Jun Zhao, "Design, implementation, and performance of the Astro-H SXS calorimeter array and anticoincidence detector," *J. Astron. Telesc. Instrum. Syst.* **4**(1), 011214 (2018), doi: 10.1117/1.JATIS.4.1.011214.

Design, implementation, and performance of the Astro-H SXS calorimeter array and anticoincidence detector

Caroline A. Kilbourne,^{a,*} Joseph S. Adams,^{a,b} Regis P. Brekosky,^{a,c} James A. Chervenak,^a Meng P. Chiao,^{a,b} Megan E. Eckart,^a Enectali Figueroa-Feliciano,^d Masimiliano Galeazzi,^e Christoph Grein,^f Christine A. Jhabvala,^a Daniel Kelly,^{a,g} Maurice A. Leutenegger,^{a,b} Dan McCammon,^h F. Scott Porter,^a Andrew E. Szymkowiak,ⁱ Tomomi Watanabe,^{a,j} and Jun Zhao^f

^aNASA Goddard Space Flight Center, Greenbelt, Maryland, United States

^bUniversity of Maryland, Center for Space Sciences and Technology, Baltimore County, Baltimore, Maryland, United States

^cMEI Technologies, Inc., Houston, Texas, United States

^dNorthwestern University, Department of Physics, Evanston, Illinois, United States

^eUniversity of Miami, Department of Physics, Coral Gables, Florida, United States

^fEPIR Technologies, Inc., Bolingbrook, Illinois, United States

^gASRC Federal Space and Defense, Inc., Greenbelt, Maryland, United States

^hUniversity of Wisconsin, Department of Physics, Madison, Wisconsin, United States

ⁱYale University, Department of Physics, New Haven, Connecticut, United States

^jUniversity of Maryland, Department of Astronomy, College Park, Maryland, United States

Abstract. The calorimeter array of the JAXA Astro-H (renamed Hitomi) soft x-ray spectrometer (SXS) was designed to provide unprecedented spectral resolution of spatially extended cosmic x-ray sources and of all cosmic x-ray sources in the Fe-K band around 6 keV, enabling essential plasma diagnostics. The SXS had a square array of 36 x-ray calorimeters at the focal plane. These calorimeters consisted of ion-implanted silicon thermistors and HgTe thermalizing x-ray absorbers. These devices demonstrated a resolution of better than 4.5 eV at 6 keV when operated at a heat-sink temperature of 50 mK. We will discuss the basic physical parameters of this array, including the array layout, thermal conductance of the link to the heat sink, resistance function, absorber details, and means of attaching the absorber to the thermistor-bearing element. We will also present the thermal characterization of the whole array, including thermal conductance and crosstalk measurements and the results of pulsing the frame temperature via alpha particles, heat pulses, and the environmental background. A silicon ionization detector was located behind the calorimeter array and served to reject events due to cosmic rays. We will briefly describe this anticoincidence detector and its performance. © The Authors. Published by SPIE under a Creative Commons Attribution 3.0 Unported License. Distribution or reproduction of this work in whole or in part requires full attribution of the original publication, including its DOI. [DOI: [10.1117/1.JATIS.4.1.011214](https://doi.org/10.1117/1.JATIS.4.1.011214)]

Keywords: microcalorimeter; x-ray calorimeter; anticoincidence detector; Astro-H; Hitomi; x-ray spectroscopy.

Paper 17048SSP received Aug. 15, 2017; accepted for publication Jan. 19, 2018; published online Feb. 23, 2018.

1 Introduction

An x-ray calorimeter provides extremely high spectral resolution by measuring the energy of each incoming photon after it has thermalized in a low-heat capacity absorber. The 36-pixel calorimeter array of Suzaku XRS¹ was based on micromachined, deep-diffused, ion-implanted silicon thermometers,² and separately attached HgTe x-ray absorbers.^{3,4} The pitch of the XRS array was 0.64 mm, but an alternate thermistor-array design with 0.83-mm pitch was successfully fabricated and considered for flight as an option for increasing the field of view at the cost of worse spectral resolution. The array for the Hitomi soft x-ray spectrometer (SXS) was selected from these alternate XRS thermistor arrays, but several important modifications that were implemented for SXS made even better energy resolution than XRS possible.

There were three significant improvements made to the fabrication and operation of the calorimeter array between XRS and SXS: (1) the change of the heat-sink temperature from 60 to

50 mK, (2) development of HgTe absorbers with lower specific heat, and (3) improved heat sinking of the calorimeter array die. These improvements enabled the typical resolution at 6 keV to improve from 5.5 eV full-width at half-maximum (FWHM) to 4 eV FWHM, despite the 70% larger absorber area. Early results from the use of the improved absorbers were presented elsewhere,^{5,6} but here we present more detail on this and the other improvements.

The anticoincidence (anti-co) detector was a Si ionization detector designed to operate at 50 mK. The SXS anti-co was a spare component from XRS, mounted to a different fan-out board, which was modified for reasons unrelated to anti-co performance.

This paper is one of a series of papers about the instrumentation of Hitomi organized for coordinated publication. This particular paper is primarily concerned with the changes made to the design of the SXS detectors, relative to the XRS detectors, with the goal of presenting the resulting nearly intrinsic performance of the sensors themselves, and not of the SXS instrument as a whole, either on the ground or in orbit. This is an unattainable goal, as every test platform and every environment leaves its imprint on the performance, thus we also provide an

*Address all correspondence to: Caroline A. Kilbourne, E-mail: caroline.a.kilbourne@nasa.gov

estimate for how much the typical measured resolution was degraded by the system and the environment. Discussion of in-orbit results pertaining to the improved heat sinking is unavoidable in this paper, as cosmic-ray effects motivated the change, the effectiveness of which could not be evaluated on the ground, but other papers discuss overall instrument performance, in-orbit operations, and in-orbit performance more generally. Yet other papers in the collection present calibration and details of the various SXS subsystems.

2 Design Process

When the SXS was designed as a replacement for the XRS, much of the legacy design of the detector system was reused, to minimize cost and risk. An increase in focal length for SXS was matched by using the alternate array layout from XRS, such that the angular extent of each pixel remained 0.5 arcmin. The potential degradation in resolution from the larger-volume x-ray absorber on each pixel was offset by reducing the specific heat of the absorber and operating at lower temperature. Several batches of thermistor arrays with the alternate pitch had been fabricated with slightly different temperature sensitivity. Thus, the design of the SXS calorimeter came from the optimization of a few choices within tight constraints.

When the XRS 6×6 arrays were designed, the phase space was a bit larger, though fairly self-constrained. Field-of-view and spatial resolution trade off against each other because of the limited number of electrical channels, and, at a fixed pixel area, quantum efficiency and spectral resolution trade off, since thinner absorbers have lower heat capacity and, thus, better resolution. In an ideal resistive calorimeter, the resolution does not depend on resistance, thus the operating resistance is chosen to be high enough so that intrinsic thermometer Johnson noise exceeds the amplifier noise, but not higher than the resistance of practical load resistors, leading to a choice of operating point around 30 M Ω . Choice of sensitivity is related to counting rate, because the electron-phonon coupling in the thermistor becomes weaker as the thermistor temperature sensitivity is increased, and if the internal coupling in the thermometer is not greater than the coupling of the pixel to the heat sink, the effective sensitivity of the thermometer is reduced. McCammon's overview of semiconductor thermistors⁷ summarizes such hot-electron effects. The design of the XRS arrays was the product of such constrained trades, for which the parameters considered varied by no more than a factor of 2. The SXS design then evolved from the choices made for XRS.

3 X-Ray Calorimeter Pixels

High-resolution x-ray calorimeters require absorbers with low heat capacity, to allow a large increase in temperature for a given deposition of energy, yet good x-ray stopping power. In addition, the material must thermalize quickly and reproducibly so that the same deposition of energy always results in the same temperature increase, independent of where the energy is absorbed. The choice of the semimetal HgTe is a compromise among these competing requirements. Many materials have lower specific heat than HgTe but do not thermalize well.

The heat capacity of the HgTe used in the XRS calorimeter array had both a large lattice term, from its relatively low Debye temperature of ~ 145 K^{8,9} and an electronic term. The lattice term varied as T^3 and the electronic term varied as T , where T is the absolute temperature. For the XRS absorbers, the electronic term was equal to the lattice term at 0.1 K and was

roughly a factor of two higher than the lattice at the electrically biased operating point of 74 mK. Nagata et al.⁸ showed that the electronic term could be reduced by annealing HgTe in a Hg atmosphere, demonstrating that this term can be dominated by unintended doping of the material as a result of Hg vacancies. In early discussions among the teams at Goddard, EPIR Technologies, and Wisconsin, EPIR suggested that while HgTe could be produced with a negligible electronic specific heat, Hg_{0.834}Cd_{0.166}Te, the zero-bandgap composition of the HgTe/CdTe alloy, was more promising for minimizing this term because of its much lower electron effective mass.⁶ In addition, due to the higher Debye temperature of CdTe, HgCdTe also promised a slightly lower lattice specific heat.

EPIR produced samples of HgTe and HgCdTe, both grown by molecular-beam-epitaxy and annealed in Hg vapor. Both were shown to have negligible electronic specific heat. Although the HgCdTe absorbers resulted in slightly larger signals and higher signal-to-noise ratios, there was no significant difference in the spread of resolutions obtained using the two materials. Surprisingly, the HgCdTe absorbers achieved similar resolution at incident energies of 5.9, 3.3, and 1.5 keV. Frequently, when measured resolution is broader than expected from the signal-to-noise ratio, the effect can be modeled as a noise term that scales with energy. This model accounts for fluctuations in the fraction of energy that does not thermalize promptly, and it describes the broadening observed in HgTe. In the HgCdTe samples, however, the resolution was much more weakly dependent on energy. This could happen if incomplete thermalization were primarily occurring near the surface in the HgCdTe samples, which is preferentially sampled by the lower energy x-rays. Since the performance exceeded requirements for both materials, we chose HgTe because it was the simpler material and because preliminary results indicated it performed better at lower energies. Figure 1 shows the distribution of resolutions at 5.9 keV in test devices with both HgTe and Hg_{0.834}Cd_{0.166}Te absorbers. The pixels used had similar temperature sensitivity. The Hg_{0.834}Cd_{0.166}Te histogram is displaced vertically for clarity.

For XRS, the HgTe material was mechanically diced to form the square absorbers, leading to possible damage at the boundaries. For SXS, EPIR delineated the absorbers via a dry etch. In addition, a serial number was etched into each absorber. This number was useful to identify absorbers in a package after visual screening. If there had been non-uniformity in the HgTe layers, good and bad regions could have been identified by number. As done for XRS, the absorbers were attached by hand with epoxy to polymer stand-offs on each suspended thermistor. The stand-offs were made of SU-8, a negative epoxy photoresist manufactured by MicroChem. The process was assisted by a micrometer-controlled XYZ stage and a microscope. Figure 1(a) shows one of the flight-candidate arrays for SXS after some of the absorbers had been placed. The pixel pitch was 0.832 mm. The identifying numbers on the absorbers are on the downward facing side, because the dry etch left the sidewalls slightly beveled and the tight positioning tolerance required that the widest face be on top. The typical width of the top face was 0.819 mm. Both SXS and XRS were designed for absorber quantum efficiency at 6 keV greater than 95% and fill factors greater than 95%.

When an x-ray photon warms a pixel, the change in resistance causes a change in the voltage drop across the sensor. We have constructed a detector model that includes the

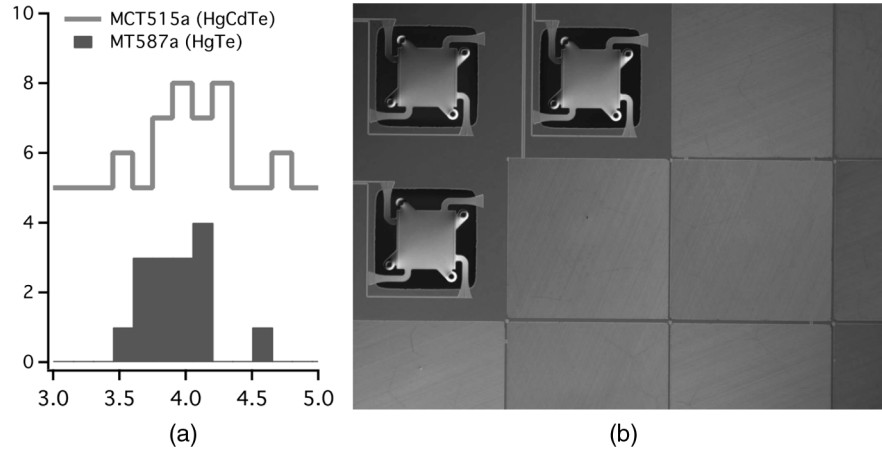


Fig. 1 (a) Accumulated resolution statistics for tests of absorbers made of annealed HgTe and $\text{Hg}_{0.834}\text{Cd}_{0.166}\text{Te}$. The distributions were nearly identical despite the lower specific heat of the $\text{Hg}_{0.834}\text{Cd}_{0.166}\text{Te}$. The histogram of $\text{Hg}_{0.834}\text{Cd}_{0.166}\text{Te}$ results has been displaced upward for clarity. (b) Portion of a flight-candidate array after several absorbers have been placed. Three suspended thermistors without absorbers can be seen in the upper left of the photograph. All of the suspended silicon structure is 0.0015 mm thick. The absorbers are glued to 0.01-mm tall SU-8 tubes on the four tabs around each thermistor. Also visible are the four silicon support beams that provide controlled thermal isolation between the thermistor and the heat sink. The pixel pitch is 0.832 mm and the typical width of the front face of an absorber was 0.819 mm.

resistance as a function of temperature $R(T)$, the absorber and thermistor heat capacities, the thermal conductances (of the links between the absorber and thermistor, between the thermistor electrons and phonons, and of the 1.5- μm -thick Si beams between the thermistor and thicker silicon containing the array), the load resistor that is in series with the thermistor and the bias voltage applied, and assorted other terms such as stray capacitance, power loading from stray infrared radiation, and circuit noise. The characterizations of the SXS detectors did not completely fix the values of all of these parameters. In particular, fits to current–voltage measurements determined a lower value for the thermal conductance of the support beams than appeared to best describe the pulse shapes and heights. Table 1 lists some of the key parameters for the XRS and SXS devices to compare them qualitatively, although some values may be refined with further work. The cited values for the spectral resolution at 5.9 keV are representative measured values for pixels across the two arrays during tests at the instrument level and lower levels of integration. As such, they include nonlinearity and some degree of laboratory interference. There were no apparent intrinsic excess noise terms in either array, but both displayed energy-dependent excess broadening relative to the baseline resolution inferred from processing data records without pulses. At 6 keV, the excess broadening represented a noise term of 2 to 3 eV, added in quadrature with the baseline resolution, presumably due to slight variation in thermalization within the absorber. For SXS, the intrinsic resolution due to the detector itself was estimated to be about 3.8 eV.

Ideally, the resistance in a doped semiconductor at low temperatures will be governed by the equation for variable range hopping in the case of a Coulomb gap:¹⁰ $R(T) = R_0 \exp[(T_0/T)^{0.5}]$, where R_0 and T_0 are constants. However, deviations at low temperatures have been reported,¹¹ and various empirical expansions of the resistance function, with more or less physical justification, have been used to describe the behavior. In Table 1, rather than quote parameters of one resistance function or another, we cite simply α , where $\alpha = \partial \log(R)/\partial \log(T)$ at the operating temperature.

Table 1 Comparison of representative pixel properties of the XRS and SXS arrays.

Parameter	Suzaku XRS value	Hitomi SXS value
Heat-sink temperature	60 mK	50 mK
Operating temperature under bias	74 mK	63 mK
C of absorber at 0.1 K/operating point	0.21 pJ/K/ 0.11pJ/K	0.24 pJ/K/ 0.06pJ/K
G to heat sink at 0.1 K/operating point	160 pW/K/ 60 pW/K	130 pW/K/ 28 pW/K
R at operating point	27 M Ω	34 M Ω
$\alpha = \partial \log(R)/\partial \log(T)$	-7.0	-6.3
Pulse fall time	3.5 ms	3.5 ms
Typical energy resolution at 5.9 keV, instrument ground testing	5.7 eV	4.2 eV

4 Thermal Properties of the Entire Array

4.1 Additional Heat-Sinking Gold and Its Limitations

The Suzaku XRS array was thermally anchored via an epoxy bond to an alumina board connected to the heat sink via gold wire bonds. The weak coupling of this epoxy bond resulted in several nonideal effects. Gain and resolution depended on the x-ray flux incident on the array. The resolution also depended on the cosmic-ray rate through particle interaction with the frame, and large energy deposition (>200 keV) into the frame produced a temperature pulse big enough to cause signal pulses

on many pixels simultaneously, wasting telemetry bandwidth. In order to minimize these effects on the Astro-H SXS array, a thick gold layer was added to the frame of the array to increase its heat capacity and to permit heat sinking via gold wire bonds. Specifically, electron-beam-evaporated gold ($1.5\ \mu\text{m}$) was deposited in areas on the front and back through shadow masks. In the case of the backside deposition, the chips were angled to avoid deposition on the suspended thermistors. Gold wire bonds were used to thermally connect the top-side gold to the gold of the alumina fan-out board. The montage of Fig. 2 shows the back and front Au layers and the Au ribbon bonds of the spare SXS array.

To characterize arrays in both the XRS and SXS style, we attached additional heaters and thermometers to the frame and fan-out board of sample devices. The XRS arrays were bonded with epoxy to alumina boards, the thick gold coating of which was connected to the heat sink via gold wire bonds (40 bonds, 3 mm long, 0.025 mm diameter). We typically

measured $G = 10^{-7}\ \text{W/K}$ from the array to the board, and $10^{-5}\ \text{W/K}$ from the board to the heat sink at 60 mK. Replicating the heat-sinking wire-bond interface at the array thus initially appeared to have the potential to improve the heat sinking by two orders of magnitude.

However, there are other thermal interfaces that need to be considered. Each gold triangle on the front of the SXS array covers $\sim 8\ \text{mm}^2$. If the electron-phonon coupling constant $\Sigma = 1.4 \times 10^9\ \text{W/K}^5\ \text{m}^3$ (as we have measured in other devices), then for volume V , $G_{\text{ep}} = 5V\Sigma T^4 = 5 \times 10^{-7}\ \text{W/K}$ for $1.5\text{-}\mu\text{m}$ Au at 50 mK. Using the Au/Si boundary conductance of Swartz and Pohl,¹² the thermal conductance from the frame into each Au triangle = $6 \times 10^{-7}\ \text{W/K}$. For a residual resistivity ratio ~ 6 , the thermal conductance across one of the Au triangles is also $\sim 10^{-6}\ \text{W/K}$. If we assume a 1-mm mean-free path for the underlying silicon (0.38 mm thick), then the conduction between the frontside and backside gold in each area of overlap $\sim 2 \times 10^{-6}\ \text{W/K}$.

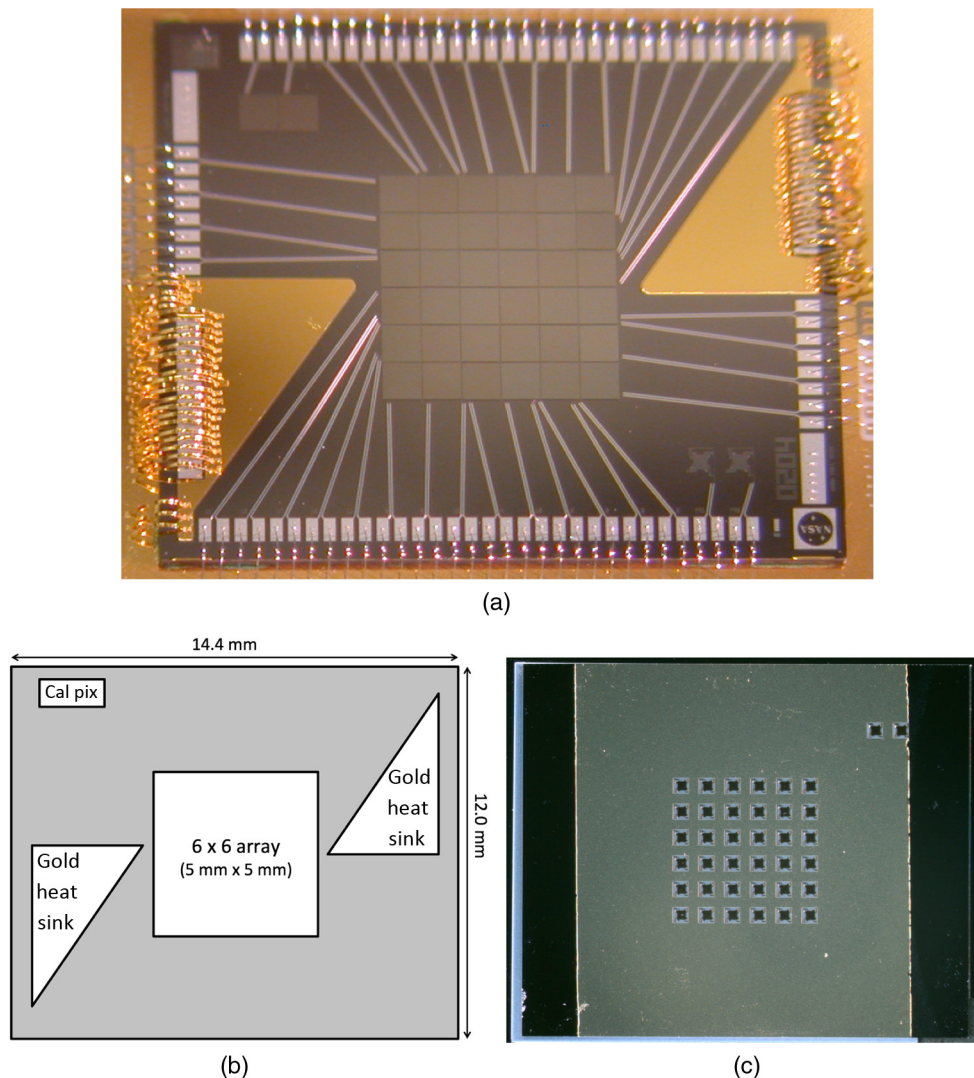


Fig. 2 (a) Finished SXS spare array, with heat sinking, wire bonds, and absorbers. One pixel of the central 6×6 array was not read out, and one of two pixels located outside of the aperture (in the upper left corner in the photograph) was wired in its place to serve as a calibration reference. A collimated ^{55}Fe source continuously illuminated that pixel, providing a monitor of the gain and the line-spread function. (b) Guide to photograph at top, showing extent of the 6×6 array of calorimeter pixels, the overall size of the die, and the areas of the front-side heat sinking. (c) Backside layer of Au.

The following list summarizes these order-of-magnitude estimates of the relevant thermal conductances that contribute to the array-scale thermal response, and Fig. 3 shows a cartoon layout of their arrangement. In the figure, use of the resistor symbol within a block indicates conduction through the body, and multiple connections between bodies indicate an extended interface.

- Gold wire bonds: $\sim 10^{-5}$ W/K
- Electron–phonon in top film: $\sim 10^{-6}$ W/K
- Au/Si boundary: $\sim 10^{-6}$ W/K
- Au conduction: $\sim 2 \times 10^{-6}$ W/K
- Top/bottom conduction in Si: $\sim 4 \times 10^{-6}$ W/K
- Si/epoxy: $\sim 10^{-7}$ W/K (parallel)

Looking at these values and the layout of Fig. 3, it becomes clear that an increase in the thermal conductance to the gold on the alumina board by less than a factor of 10 should be expected. In fact, measurements of the heat sinking on arrays with large differences in the number, length, and cross-sectional area of the gold wire bonds repeatedly resulted in $G = 6$ to 8×10^{-7} W/K, consistent with the various interface terms dominating G . While this presages the challenges of heat sinking large arrays in future instruments, the improvement over XRS is nonetheless substantial, despite the constraints of working within a pre-existing layout. The nominal heat capacity of the added Au at 50 mK is 8×10^{-10} J/K, thus we expected the cooling time constant for the whole chip to be 1 ms.

4.2 Thermal Crosstalk

Thermal crosstalk is another phenomenon dependent on the heat sinking of the array. Even XRS had no triggerable thermal crosstalk from x-ray absorption on other pixels, but small crosstalk pulses contributed to a rate-dependent (and spectrum-dependent) noise. On XRS, the nearest-neighbor crosstalk (as determined from record averaging) was a factor of three higher than from other pixels, but beyond that immediate radius the

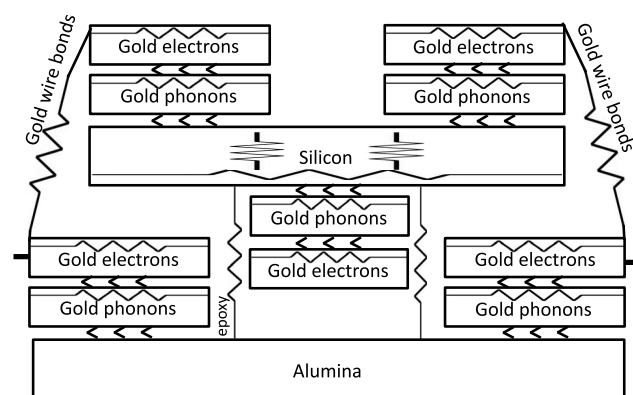


Fig. 3 Schematic of the thermal interfaces in the calorimeter array. Use of the resistor symbol within a block indicates conduction through the body, and multiple connections between bodies indicate an extended interface. The silicon chip is represented by the silicon block in the center. The gold of the alumina board is heat sunk to the 50-mK stage via wirebonds. The thermal path to that point from the silicon involves many interfaces. For example, heat in the middle of the array makes use of the underside gold to diffuse to the outer part of the frame, but then needs to go through multiple interfaces to reach the top-side gold where the wire-bond contact is made.

crosstalk fraction flattened out, showing that the energy of a pulse could diffuse throughout the frame around the array before the frame would begin to cool appreciably.

For the SXS array, we measured the thermal crosstalk in the same way as for XRS, using the 59.5 keV gamma rays from ^{241}Am to impart a thermal impulse into the trigger channel, and averaging the simultaneous records on other pixels to look for crosstalk. The crosstalk fraction was determined from comparison of the crosstalk pulses to the response of each pixel to 5.9 keV, scaling from the 59.5 keV input. The results of these measurements are shown in Fig. 4 and tabulated in Table 2. Figure 4 shows that thermal-crosstalk pulses rise more slowly than signal pulses, becoming smaller and rising increasingly more slowly the greater the distance from the trigger event. Note that the XRS equivalent values listed in Table 2 are not individual measurements for the exact pairs measured in the SXS but merely reflect the observation that the XRS thermal crosstalk had an approximately binary response, with one value for nearest neighbors and all others roughly one-third of that value. The thermal crosstalk in SXS was not only less than observed in XRS but also continued to fall off with distance, merging with the noise in the furthest pixels (for 220 averaged records each). The SXS arrays benefited not only from the gold deposited on the back but also from the thicker silicon between pixels that was a consequence of the larger pitch. Analysis of high-count-rate data indicated that the dependence of gain and resolution on flux was greatly diminished.

4.3 Thermal Response to Cosmic-Ray Interactions in the Frame of the Array

In ground testing of the Suzaku XRS array, we identified groupings of simultaneous signals resulting from cosmic rays depositing energy in the silicon frame of the array.¹³ The rise times of these pulses were similar to the rise times of x-ray events, thus they could only be identified by coincidence screening. In orbit, the rate of these clustered events tracked the orbital variation in the rate of events in the anticoincidence detector. Since a majority of the pixels triggered for each of these frame events, the XRS telemetry was full of them, and events too small to trigger degraded the energy resolution of the x-ray events.^{1,14}

In ground testing of the SXS prototype arrays, there were so few clustered events that it was not possible to assess positively whether they were the same phenomenon on a different scale or due to some other environmental interference. Exposure of the frame of a test device to alpha particles from ^{241}Am did not produce any triggers. Heater pulses simulating energy impulses to the frame of 161 and 446 MeV produced large slow events on multiple pixels at a scale apparently consistent with the lack of triggers from 5 MeV alpha particles.

In orbit, SXS data clearly showed correlated events as on XRS, but at a much lower rate. Figure 5 illustrates the difference. The top two panels show 90 min of XRS background data, with the top covering 0 to 10 keV and the middle covering 0 to 0.5 keV. The bottom panel shows 90 min of SXS data. In all panels, the right-hand axis gives the anticoincidence rate (solid curve), which is plotted as an indicator of the incident particle rate. Comparing XRS and SXS over the same energy range, the SXS data contain far fewer grouped events. Interestingly, the SXS distribution of events from 0 to 0.5 keV looks similar to the XRS distribution over the 0 to 10 keV band, as if the same input distribution resulted in events smaller in SXS by a factor of 20. The SXS frame events are generally more slowly

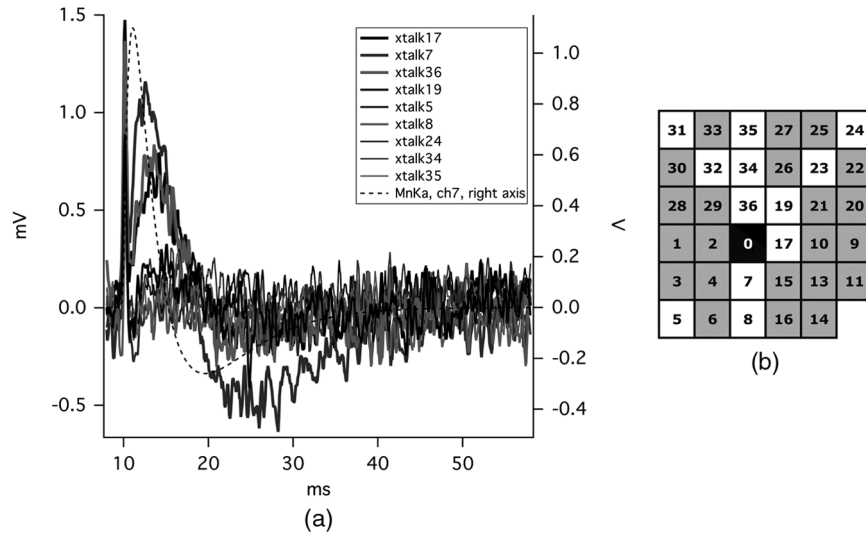


Fig. 4 (a) Averaged thermal crosstalk pulses, overlaid with the response to a 6 keV x-ray. Pulses represent a subset of the channels included in Table 2. (b) Channel map: the group trigger was based on 59.5-keV gamma-ray events on channel 0. The pixels indicated in white correspond to the crosstalk measurements of Table 2.

rising and falling than the ones on XRS. There are some clustered events that have faster rise times, but where pulse data are available we see that these are small pulses with spikes or large pulses with ringing at the rise, but the rest of the pulse is slow.

Table 2 Thermal crosstalk intensity for SXS, compared with XRS. Channel numbers correspond to the numbering in the array schematic of Fig. 4. Note that the XRS equivalent values listed are not individual measurements for the exact pairs measured in the SXS, but merely reflect the observation that the XRS thermal crosstalk had an approximately binary response, with one value for nearest neighbors and all others roughly one-third of that value.

Channel number	Relationship	Fraction of trigger	XRS equivalent
7	Nearest neighbor, exterior	$9.5E - 05$	$7.0E - 04$
17	Nearest neighbor, interior	$5.1E - 05$	$7.0E - 04$
36	Nearest neighbor, interior	$5.5E - 05$	$7.0E - 04$
19	Diagonal neighbor	$1.8E - 05$	$2.5E - 04$
34	Second-nearest neighbor	$9.0E - 06$	$2.5E - 04$
32	Second and diagonal	$1.3E - 05$	$2.5E - 04$
23	Second along diagonal	$9.1E - 06$	$2.5E - 04$
8	Second-nearest neighbor, edge	$<1E - 5$	$2.5E - 04$
5	Second along diagonal, edge	$<1E - 5$	$2.5E - 04$
35	Third-nearest neighbor, edge	$1.1E - 05$	$2.5E - 04$
31	Third and diagonal, edge	$<1E - 5$	$2.5E - 04$
24	Far corner	$<1E - 5$	$2.5E - 04$

We report on our extensive investigation of the correlated background events of SXS in Ref. 15.

In Ref. 15, we also report on a small but significant correlation of the resolution of the calibration pixel (see Fig. 2 and its caption) with geomagnetic cut-off rigidity (COR) and, hence, cosmic-ray rate. The spread in FWHM resolution ranged from 4.7 to 5.1 eV, and, although part of that must be due to cosmic-ray interaction with the control thermometer, initial simulations indicated that thermal noise from the many frame events too small to trigger is likely the predominant cause. The implied resolution in the absence of cosmic rays is about 4.4 eV; note that this analysis presumes that the impact of changing interference from spacecraft systems averages out over each COR range analyzed.

Figure 6 shows three pulses from a typical frame event, compared with a representative x-ray pulse. The frame pulses are about a factor of 3 slower rising, and they resemble the pulses produced on test devices when a heat pulse was put into the frame. Correcting the pulses for the ac coupling of the amplifier, we find that the thermal decay time is 7 ms, a factor of 2 slower than expected from the nominal heat capacity of the Au heat sinking and the measured static thermal conductance from the detector frame to the thermal sink. With the expected frame response time of 1 ms, the frame events should have decayed with close to the pixel time constant of 3.5 ms. The factor of 20 reduction in sensitivity, compared with XRS, to energy deposited in the frame resulted from the combination of the higher thermal conductance of the frame heat sinking, the higher heat capacity of the frame, internal time constants on the frame, and the interaction of the signal processing with the slower pulses.

5 Anticoincidence Detector

The anticoincidence detector used for SXS was an XRS spare with no alterations made to the detector die itself. Details of the design can be found in Ref. 1. The sensor was a $1 \text{ cm}^2 \times 0.5 \text{ mm}$ ionization detector made from high-purity Si configured as a p-i-n diode but with the intrinsic carriers

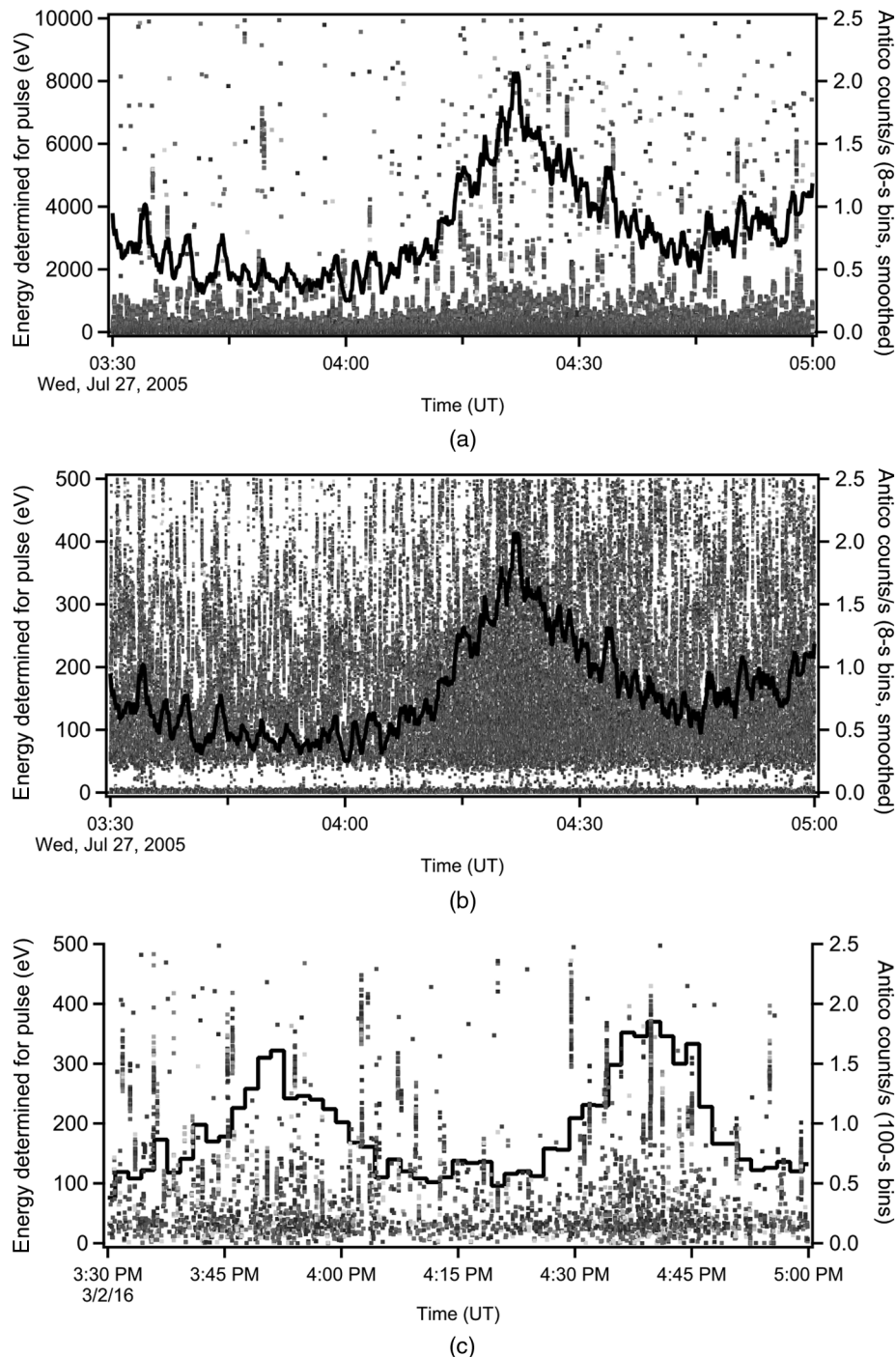


Fig. 5 Correlated background events on (a, b) XRS and (c) SXS. In all plots, the right-hand axis gives the antiproton rate (solid curve), which is plotted as an indicator of the cosmic-ray rate. Each point is the energy of a calorimeter event (left axis), shaded according to pixel number.

completely frozen out. A nominal bias of 6 V was dropped across the sensor and a load resistor, and the voltage dropped across the load resistor by the ionization current was monitored by two read-out channels for redundancy.

Several changes were made to how the antiproton detector was read out for SXS. The decay time of the anti-co pulses is set by the total capacitance (intrinsic and parasitic) and the load resistor. The intrinsic pulse height is independent of the choice of load resistor. The faster the pulse, however, the wider the bandwidth needed in the shaping filter, thus the worse

the signal-to-noise ratio for a measurement of the peak voltage. Therefore, the choice of pulse fall time is determined by balancing the needs for a low threshold energy and low dead time. On XRS, with a 25-keV trigger, the average rate at the anti-co was 0.9/s outside of SAA, but it went up to 2/s in portions of the orbit with low geomagnetic COR. To achieve 99% efficiency at 2/s, we need a dead time of <5 ms per event. To match the modeled and expected geometric/energy-cut efficiency of 99.8%, a dead time <1 ms is required. If a typical event is 0.5 MeV, we need about five exponential time constants to get down to the

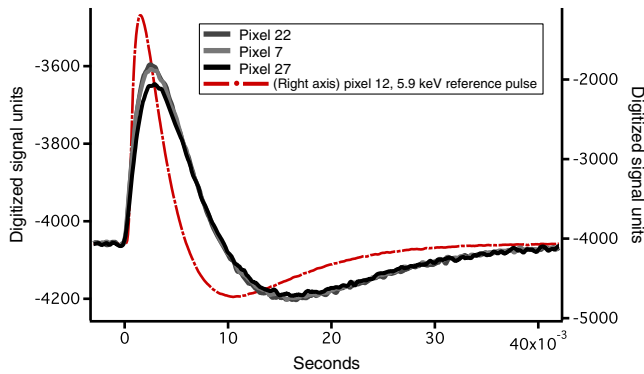


Fig. 6 Three pulses from an apparent frame event in SXS in-orbit data (scale on left axis, digitized signal units), compared with the shape of a normal x-ray event (right axis).

noise level. An XRS anti-co pulse had a fall time of 0.3 ms. For SXS, we changed the load resistor value from 5 to 2.5 M Ω to reduce the time constant to 0.15 ms, and the dead time to <1 ms. The noise corresponded to an FWHM resolution of 1.7 keV.

On XRS, the anti-co signals were used for on-board flagging of calorimeter events, but pulse-height data from the anti-co were not telemetered. For SXS, anti-co events were included in the telemetry. Although the anti-co signal is faster than the calorimeter signal, it was sampled at the same rate (12,500 samples/s) as the calorimeters. The coarse sampling results in an FWHM resolution degradation of 6% of the peak energy, in addition to intrinsic energy dependence. This term will dominate the anti-co intrinsic resolution at energies above ~ 300 keV, but it does not affect the trigger sensitivity, which is the most important attribute. The resolution measured at 22 keV was 2.5 keV and at 60 keV was 4.1 keV.

Based on GEANT simulations, we previously determined¹⁶ that an anti-co threshold of 100 keV would be the highest acceptable. The SXS anti-co had abundant margin against that requirement. In SXS ground testing, we were able to set the anti-co threshold to ~ 6 keV but raised it to ~ 10 keV to minimize triggering on x-rays.

6 Conclusions

The Hitomi SXS array was not simply a spare part from Suzaku XRS, but rather the highly successful implementation of lessons learned from the former program. The Hitomi SXS calorimeter array worked extremely well and exceeded its requirement for energy resolution. Achieving <5 eV resolution on such large pixels (0.83 mm) required developing a process that produced HgTe absorber material with specific heat very close to the theoretical value for this material and developing a scheme for heat sinking the array so that cosmic rays did not create significant thermal fluctuations. The performance of the array represents the convergence toward the asymptotic limit of ion-implanted thermistor calorimeter technology.

Disclosures

This paper was based on our contribution to the proceedings of the SPIE Astronomical Telescopes and Instruments meeting held in Edinburgh, United Kingdom, in June 2016.¹⁷

References

1. R. L. Kelley et al., "The Suzaku high resolution x-ray spectrometer," *Publ. Astron. Soc. Jpn.* **59**, S77–S112 (2007).
2. R. P. Brekosky et al., "Fabrication process responsible for fundamentally improving silicon x-ray microcalorimeter arrays," *Nucl. Instrum. Methods Phys. Res., Sect. A* **520**, 439–442 (2004).
3. C. K. Stahle et al., "The next generation of silicon based x-ray microcalorimeters," *Proc. SPIE* **4851**, 1394–1403 (2003).
4. C. K. Stahle et al., "The next-generation microcalorimeter array of XRS on Astro-E2," *Nucl. Instrum. Methods Phys. Res., Sect. A* **520**, 466–468 (2004).
5. F. S. Porter et al., "The detector subsystem for the SXS instrument on the Astro-H observatory," *Proc. SPIE* **7732**, 77323J (2010).
6. P. Dreiske et al., "Molecular beam epitaxially grown HgTe and HgCdTe-on-silicon for space-based x-ray calorimetry applications," *J. Electron. Mater.* **39**, 1087–1096 (2010).
7. D. McCammon, "Semiconductor thermistors," in *Cryogenic Particle Detection*, C. Enss, Ed., Topics in Applied Physics, Vol. **99**, pp. 35–61, Springer-Verlag, Berlin, Heidelberg (2005).
8. S. Nagata et al., "Magnetic-susceptibility, specific-heat, and the spin-glass transition in Hg_{1-x}Mn_xTe," *Phys. Rev. B* **22**, 3331 (1980).
9. J. G. Collins et al., "Thermal-expansion of ZnTe And HgTe and heat-capacity of HgTe at low-temperatures," *J. Phys. C: Solid State Phys.* **13**, 1649–1656 (1980).
10. A. L. Efros and B. I. Shklovskii, "Coulomb gap and low-temperature conductivity of disordered systems," *J. Phys. C: Solid State Phys.* **8**, L49–L51 (1975).
11. J. Zhang et al., "Hopping conduction in partially compensated doped silicon," *Phys. Rev. B* **48**, 2312–2319 (1993).
12. E. T. Swartz and R. O. Pohl, "Thermal boundary resistance," *Rev. Mod. Phys.* **61**, 605–668 (1989).
13. C. K. Stahle et al., "Cosmic ray effects in microcalorimeter arrays," *Nucl. Instrum. Methods Phys. Res., Sect. A* **520**, 472–474 (2004).
14. C. A. Kilbourne et al., "Analysis of the Suzaku/XRS background," *Nucl. Instrum. Methods Phys. Res., Sect. A* **559**, 620–622 (2006).
15. C. A. Kilbourne et al., "In-flight calibration of Hitomi soft x-ray spectrometer. 1. Background," *Publ. Astron. Soc. Jpn.* **70**, 18 (2018), in press.
16. T. Saab et al., "GEANT modeling of the low earth orbit cosmic ray background for the Astro-E2 XRS Instrument," *Proc. SPIE* **5501**, 320–327 (2004).
17. C. A. Kilbourne et al., "The design, implementation, and performance of the Astro-H SXS calorimeter array and anti-coincidence detector," *Proc. SPIE* **9905**, 99053L (2016).

Caroline A. Kilbourne has been developing microcalorimeters for high-resolution x-ray spectroscopy since 1987 when, as a Stanford graduate student, she adapted the NASA Goddard calorimeters for use in a hard x-ray inelastic scattering experiment. She came to Goddard as a National Research Council associate in 1992 and joined as staff in 1995. Her work with calorimeters has ranged from studies of x-ray thermalization in superconducting absorbers to the problems of heat sinking and uniformity of performance across arrays.

Biographies for the other authors are not available.